

Title: Connecting the Geometric and Electronic Structures of the Nitrogenase Iron–Molybdenum Cofactor through Site-selective Labeling

Authors: Edward D. Badding,¹ Suppachai Srisantitham,¹ Dmitriy A. Lukoyanov,² Brian M. Hoffman,² Daniel L. M. Suess^{1*}

Affiliations: ¹Department of Chemistry, Massachusetts Institute of Technology, Cambridge, Massachusetts 02139, USA; ²Department of Chemistry, Northwestern University, Evanston, Illinois 60208, USA

Contact information: *email: suess@mit.edu

Abstract: Understanding the chemical bonding in the catalytic cofactor of the Mo nitrogenase (FeMo-co) is foundational for building a mechanistic picture of biological nitrogen fixation. A persistent obstacle in these efforts has been that the ⁵⁷Fe-based spectroscopic data—although rich with information—reflects all seven Fe sites, and it has therefore not been possible to map individual spectroscopic responses to specific sites in the 3-D structure. We herein overcome this challenge by incorporating ⁵⁷Fe into a single site of FeMo-co. Spectroscopic analysis of the reduced and oxidized forms of the resting state provides unprecedented insights into the local electronic structure of the terminal (Fe1) site, including its oxidation state and spin orientation. This leads to the discovery that Fe1 is a site of redox reactivity during oxidation of the resting state, and on this basis, we suggest a possible role for Fe1 as an electron reservoir during N₂ reduction catalysis.

Main Text

Introduction

Nitrogenases catalyze the reduction of N_2 to NH_3 (Fig. 1A), and, along with the Haber–Bosch process, are responsible for producing the vast majority of the fixed nitrogen that supports life on Earth.¹⁻³ Although the multi-electron, multi-proton generation of NH_3 from N_2 is thermodynamically favorable under ambient conditions, it is kinetically very challenging because the first step, cleavage of the $\text{N}\equiv\text{N}$ triple bond, is so unfavorable. As a result, the mechanism of biological N_2 fixation—particularly the chemistry that occurs at FeMo-co, the catalytic cofactor of the dominant Mo-nitrogenase isozyme—has been intensively studied for decades.³⁻⁸ Foundational to this inquiry is an understanding of FeMo-co's electronic structure: the distribution and coupling of the valence electrons in the resting state, and how the electronic structure changes throughout the catalytic cycle. However, the sheer number of open-shell metal ions in FeMo-co (seven structurally unique Fe sites and one Mo center⁹) pushes the limits of computational analysis¹⁰⁻¹⁶ and, as described below, presents a number of challenges in its experimental characterization.

Whereas the Mo center in FeMo-co can be selectively probed using Mo-specific spectroscopic techniques (*e.g.*, Mo X-ray absorption methods and ⁹⁵Mo electron-nuclear double resonance (ENDOR) spectroscopy),¹⁷⁻²³ the individual Fe centers are more difficult to study. In particular, the wealth of information contained in the ⁵⁷Fe Mössbauer and ENDOR spectra—including the Fe oxidation states, the covalency of Fe–S/C and Fe–Fe/Mo interactions, the local spin states, and the orientations of the local spins with respect to the total spin—has been challenging to extract because the ⁵⁷Fe spectroscopic data cannot be mapped onto the geometric structure (Fig. 1B). Even for the most well-characterized state, the reduced resting state ('M^N'), it has not been possible to experimentally correlate the crystallographically observed Fe sites (Fe1–Fe7; Fig. 1B/C)⁹ to the spectroscopically observed ⁵⁷Fe sites (A^1 - A^4 , B^1 - B^2 , where the A and B sites have negative and positive a_{iso} , respectively, and the B^1 site represents two equivalent Fe

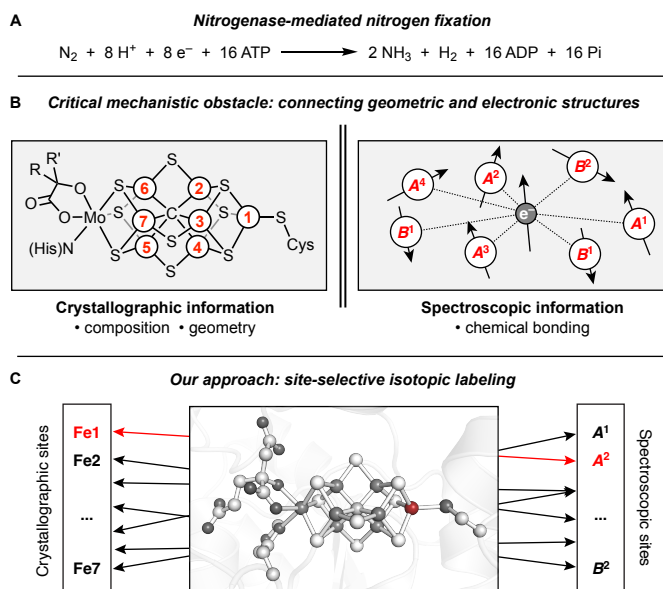


Figure 1. Employing site-selective isotopic labeling to understand the mechanism of biological nitrogen fixation. A) The reaction performed by the Mo nitrogenase is kinetically challenging and mechanistically complex. B) A major challenge in mechanistic studies of nitrogenases is the inability to correlate spectroscopic data to geometric structure. Numbers correspond to the crystallographically defined Fe sites (Fe1-Fe7). R = $-\text{CH}_2\text{CO}_2^-$; R' = $-(\text{CH}_2)_2\text{CO}_2^-$. C) Site-selective labeling as a strategy to connect the geometric and electronic structures of FeMo-co. PDB accession code: 3U7Q⁹

centers; Fig. 1B/C).^{20,24-26} For ^{57}Fe Mössbauer spectroscopy in particular, these challenges are compounded by poor resolution of the complex set of overlapping signals arising from the seven Fe sites. Building on prior ENDOR and Mössbauer studies, Yoo and coworkers undertook what still remains the most comprehensive Mössbauer spectroscopic analysis of FeMo-co;²⁵ although this work yielded a working set of Mössbauer parameters that have been widely employed in computational analysis, the authors acknowledge both the difficulties in simulating the Mössbauer data due to the poor resolution and the limitations of their interpretation owing to the inability to assign the spectroscopic features to specific sites in the structure. More broadly, few experimental methods have been used to connect the spectroscopic and structural properties of FeMo-co,²⁷ and this has been a persistent obstacle in efforts to understand the mechanism of biological nitrogen fixation.

Our strategy for overcoming these challenges is to selectively enrich individual Fe sites of FeMo-co with ^{57}Fe (Fig. 1C). Analysis of such samples would simultaneously overcome issues of poor

spectroscopic resolution and provide site-specific information on the chemical bonding at individual Fe centers. We recently reported²⁸ the initial development of such methodology using the L-cluster, an $[\text{Fe}_8\text{S}_9\text{C}]$ cluster that is a structural analogue and biosynthetic precursor to FeMo-co.^{29,30} The L-cluster gives rise to a relatively well-resolved Mössbauer spectrum^{28,31} and was therefore ideally suited for determining the site-selectivity of our labeling protocol in these initial studies. In contrast, the seven Fe sites of FeMo-co in M^{N} give rise to sufficiently similar zero-field Mössbauer signals that they, in aggregate, appear as a single broad quadrupole doublet at temperatures above 20 K.^{25,32}

In the present work, we adapt our ^{57}Fe labeling procedure to FeMo-co and show that the terminal site of FeMo-co (Fe1) can be selectively enriched with ^{57}Fe . Characterization of this sample enables, for the first time, determination of the salient ^{57}Fe spectroscopic parameters—the ^{57}Fe Mössbauer isomer shift (δ), the ^{57}Fe Mössbauer quadrupole splitting (ΔE_{Q}), and the ^{57}Fe electron-nuclear hyperfine coupling tensor ($A(^{57}\text{Fe})$)—for a particular Fe site in FeMo-co. These findings reveal the spin orientation and yield the oxidation state of Fe1 in the M^{N} state, experimentally rule out a large number of potential electronic structures, and test predictions made in prior computational studies. We then perform a similar analysis on the spectroscopic features of the oxidized resting state (M^{OX}) and demonstrate that Fe1 is the most reduced site in the cluster and, as such, participates in redox chemistry in the interconversion of M^{N} and M^{OX} . The mechanistic consequences of these findings are discussed in the context of electron loading during catalysis.

Results and Discussion

Site-selective ^{57}Fe labeling of FeMo-co

Our approach to incorporating ^{57}Fe into the Fe1 site of FeMo-co entailed (1) using reported protocols³³ for extracting FeMo-co from the MoFe protein of the Mo nitrogenase (NifDK) into *N*-methylformamide (NMF); (2) removing the Fe1 site using a chelator; (3) reconstituting the Fe1 site with ^{57}Fe ; and (4) reinserting the labeled cofactor into apo-NifDK, a precursor to NifDK that contains the P-cluster but not FeMo-co (see Methods for details). We first studied steps (2) and (3) using EPR spectroscopy (Fig. 2). When poised in the reduced, M^{N} state (obtained by incubation with sodium dithionite (DTH)), isolated FeMo-co exhibits a broadened $S = 3/2$ signal that sharpens in the presence of thiophenol (Fig 2B, Top).³⁴ Previous work demonstrated that treatment of isolated FeMo-co with ethylenediaminetetraacetate (EDTA) eliminates the characteristic EPR signal, a process that can be reversed upon addition of Zn^{2+} .³⁵ We report here that adding excess $^{57}\text{Fe}^{2+}$ (35 equiv) to EDTA-treated FeMo-co (30 equiv of EDTA) likewise recovers the EPR signal (Fig 2B, Bottom), and based on our

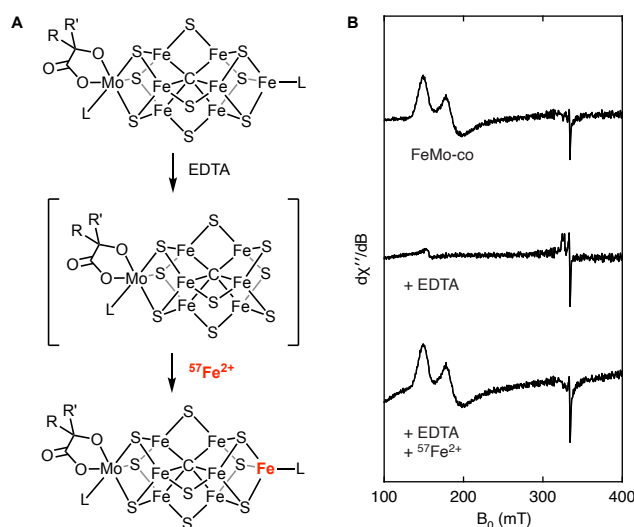


Figure 2. Postbiosynthetic incorporation of ^{57}Fe into FeMo-co. A) The chemical interconversions of isolated FeMo-co. B) Corresponding EPR spectra recorded at 9.37 GHz, 5 K, and 1 mW. All EPR samples have been incubated with DTH (2 mM) and PhSH (2 mM).

findings with the L-cluster,²⁸ we hypothesized that this protocol resulted in ⁵⁷Fe incorporation into the Fe1 site in a site-selective manner.

Encouraged by these results, we set out to prepare NifDK samples with ⁵⁷Fe in either the Fe1 site or the six belt sites (Fe2-Fe7), as well as the control sample with ⁵⁷Fe in all seven sites (Fe1-Fe7) (see Methods and the SI for details). The control sample was generated by isolating FeMo-co (M(⁵⁷Fe₇)) from fully ⁵⁷Fe-labeled NifDK, incubating the cofactor with the crude lysate from DJ1143 cells (an *Azotobacter vinelandii* strain that produces His-tagged apo-NifDK), and purifying the resulting holo-NifDK–M(⁵⁷Fe₇). Although the most common method for FeMo-co reinsertion employs purified apo-NifDK,^{25,36,37} some protocols employ crude lysate for apo-NifDK activation,^{33,38-40} and we have found that using crude lysate reproducibly gives high-quality samples with C₂H₂ reduction activity and EPR spectra that are indistinguishable from those of WT-His NifDK (see Fig. 3B and Table S13). The 80 K Mössbauer spectrum of NifDK–M(⁵⁷Fe₇) in the M^N state is consistent with previous reports^{23,25,32,34} and appears as a quadrupole doublet with an average isomer shift (δ_{avg}) of 0.39 mm s⁻¹, reflecting the overlapping signals from the seven Fe sites (*vide infra*).

We subsequently generated the site-selectively labeled samples: NifDK–M(⁵⁷Fe₆), from treating fully ⁵⁷Fe-labeled FeMo-co with EDTA followed by natural-abundance Fe²⁺; and NifDK–M(⁵⁷Fe₁), from treating natural-abundance FeMo-co with EDTA followed by ⁵⁷Fe²⁺ (Fig. 3A). These samples show full C₂H₂ reduction activity (Table S13) and cleanly exhibit the $S = 3/2$ EPR signal of native Mo-nitrogenase resting state (Fig. 3B), demonstrating that our postbiosynthetic EDTA/Fe²⁺ treatment affects neither the chemical composition of FeMo-co nor its competency for reinsertion into apo-NifDK to generate active, holo-NifDK. ICP-MS analysis of the ^{56/57}Fe content of the NifDK–M(⁵⁷Fe₁) sample indicates nearly quantitative labeling efficiency of (~90% assuming complete site-selectivity for the Fe1 site; see SI for further discussion). As discussed next, the essentially quantitative site-selectivity of ⁵⁷Fe labeling is evident in both the Mössbauer and ENDOR spectra of these samples when poised in the M^N state (Fig. 3C and 3D). Additionally, we have assessed the reproducibility of our protocol by preparing several

NifDK–M($^{57}\text{Fe}_1$) samples from different batches of FeMo-co and DJ1143 cell extract; in all cases, the samples display indistinguishable spectroscopic features (see Fig. S8) and a labeling efficiency of ~80–90% based on ICP-MS analysis.

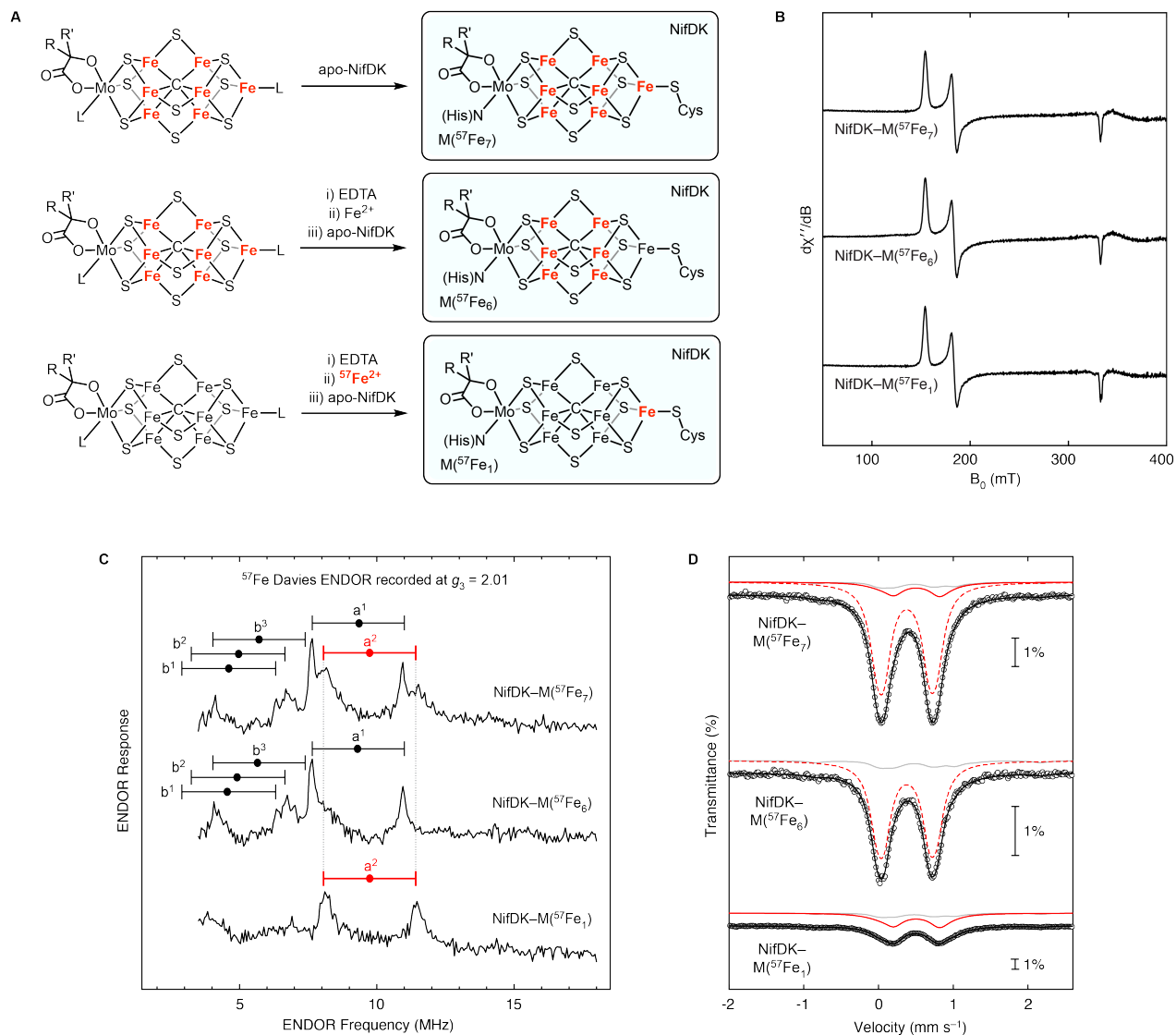


Figure 3. Preparation and characterization of site-selectively labeled holo-NifDK samples. A) Preparation of samples. B) EPR spectra recorded at 9.37 GHz, 5 K, and 1 mW. C) ^{57}Fe Davies ENDOR spectra recorded at $g_3 = 2.01$ (1235 mT), 34.745 GHz, and $T = 2$ K, with $t(\pi/2) = 40$ ns, $\tau = 600$ ns, $T_{\text{RF}} = 40$ μs , and repetition time = 15 ms. ‘Goalposts’ link doublets from individual ^{57}Fe sites, as predicted from hyperfine tensors previously reported²⁵ (see text). D) 80 K Mössbauer spectra. Circles are the experimental data; black traces are the total simulations; solid red traces are simulations of the Fe₁ site when labeled with ^{57}Fe ; dashed red traces are simulations of the belt Fe sites when labeled with ^{57}Fe ; gray traces are contributions from natural-abundance ^{57}Fe ; see the SI for details on data workup and simulation. Note that a minor high-spin Fe²⁺ site has been subtracted from the NifDK–M($^{57}\text{Fe}_1$) spectrum.

ENDOR spectroscopic analysis of the reduced resting state, M^N

The Q-band ^{57}Fe ENDOR spectra of the three nitrogenase isotopologues in the M^N state were recorded at g_3 and are shown in Fig. 3C. The spectrum of the fully ^{57}Fe -enriched sample NifDK- $M(^{57}\text{Fe}_7)$ (Fig. 3C, top) displays partially resolved signals that, as shown, are consistent with the predicted appearance of doublets from five ^{57}Fe sites, each centered at half the hyperfine coupling ($A/2$) determined from the previous analysis of X-band ENDOR spectra, and each split by twice the ^{57}Fe Larmor frequency (3.4 MHz at 1235 mT).^{20,24} (Note that although resting-state FeMo-co has $S = 3/2$, its EPR spectrum is discussed in terms of a ‘fictitious spin,’ $S = 1/2$, with g -values, $\mathbf{g} = [g_1, g_2, g_3] = [4.32, 3.62, 2.01]$).^{24,32} The corresponding spectrum of the NifDK- $M(^{57}\text{Fe}_6)$ sample in which only the Fe2-Fe7 sites are enriched with ^{57}Fe (Fig 3C, middle) retains four of those doublets, and lacks the ^{57}Fe doublet denoted a^2 , suggesting that this doublet arises from the unlabeled Fe1 site. Indeed, the assignment of this signal to Fe1 is confirmed by the spectrum of the NifDK- $M(^{57}\text{Fe}_1)$ sample, which shows only the a^2 doublet centered at the expected frequency, $A/2 = 9.8$ MHz. The absence of the a^2 doublet signal in the spectrum of NifDK- $M(^{57}\text{Fe}_6)$ highlights the efficiency of the single-site labeling, while the clean, single doublet in the NifDK- $M(^{57}\text{Fe}_1)$ spectrum underscores the high selectivity of our postbiosynthetic protocol for labeling the Fe1 site.

In the original X-band study, the ^{57}Fe ENDOR spectra were well-resolved at the low fields between $g_1 = 4.32$ and $g_2 = 3.62$ and at the high-field edge of the EPR spectrum, $g_3 = 2.01$, but poor resolution between g_2 and g_3 prevented direct experimental correlation between the responses from individual sites at the two ‘ends’ of the EPR spectrum. This ‘gap’ was addressed with ENDOR simulations, which indicated that the low-field A^2 signal evolved into the high-field a^2 doublet.²⁴ The present work confirms this correspondence between the A^2 and a^2 signals as well as the hyperfine tensor derived from the analysis of the field-dependence of the X-band ENDOR signals. The Q-band ENDOR spectra of the selectively labeled NifDK- $M(^{57}\text{Fe}_1)$ sample recorded at $g_3 = 2.01$ and $g_1 = 4.30$ (Fig. 4) display features at ~ 10 and

~16 MHz, respectively, which are reproduced (Fig. 4) using the hyperfine tensor and associated Euler angles for a single ^{57}Fe site derived from the prior ENDOR simulations: hyperfine tensor principal components written in terms of the true $S = 3/2$ spin, ${}^T\mathbf{A} = [{}^T\mathbf{A}_1, {}^T\mathbf{A}_2, {}^T\mathbf{A}_3] = [-14.0, -18.3, -19.5]$ MHz (${}^T\mathbf{A}_3$ increased by 3%) and the reported Euler angles $\alpha = 10$, $\beta = 15$, $\gamma = 0$ defining the orientation of the

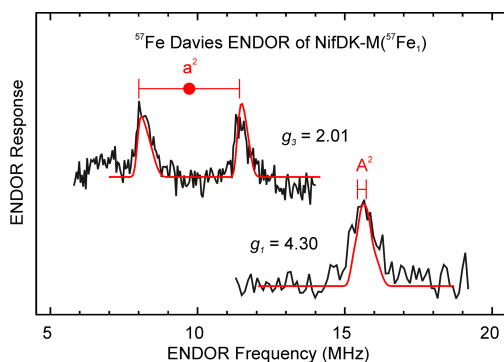


Figure 4. ^{57}Fe Davies ENDOR spectra of the NifDK–M($^{57}\text{Fe}_1$) sample recorded at $g_3 = 2.01$ (top; reproduced from Fig. 3C) and $g_1 = 4.30$ (577 mT; bottom). Center of each ‘goalpost’ equals the observed $A/2$ at that single-crystal-like g -value; breadth of each goalpost equals twice the effective nuclear Larmor frequency. At g_1 the hyperfine coupling is strongly modified by the influence of the zero-field splitting of the true-spin $S = 3/2$ resting-state FeMo-cofactor (see SI) and the *observed* Larmor splitting of the doublet at g_1 is less than predicted for an isolated ^{57}Fe site. The significance of the latter is discussed in the text. Simulations (red) carried out as before²⁵ employ parameters given in the text; experimental parameters are the same as in Fig. 3.

hyperfine-tensor frame relative to the g -tensor frame (see SI for further discussion).²⁴ Of particular importance, the observation that the *observed* Larmor splitting of the $^{57}\text{Fe}_1$ doublet at g_3 (Fig. 4) is less than would be seen for an isolated ^{57}Fe site directly reveals the negative sign of the hyperfine couplings, which in turn shows that the spin of the Fe1 site is coaligned with the overall electron spin of the cluster.²⁴ Additionally, the discovery of the $\mathbf{A}({}^{57}\text{Fe})$ hyperfine tensor corresponding to the Fe1 site is critical for both limiting the simulation space for magnetic Mössbauer experiments and delineating between the myriad broken-symmetry configurations for FeMo-co in the M^N state, as discussed below.

Mossbauer spectroscopic analysis of the reduced resting state, M^N

The 80 K Mössbauer spectra of the three NifDK isotopologues (Fig. 3A) are shown in Fig. 3D (see Methods and the SI for details on Mössbauer data collection and analysis). Each spectrum appears as a single quadrupole doublet, and the NifDK–M($^{57}\text{Fe}_7$) and NifDK–M($^{57}\text{Fe}_6$) samples are very similar (as expected), with the apparent doublet centered at $\delta_{\text{avg}} = 0.39$ and 0.38 mm s^{-1} , respectively, corresponding to the overlapping quadrupole doublets of all seven sites and the six belt sites, respectively. In contrast, the 80 K Mössbauer spectrum of NifDK–M($^{57}\text{Fe}_1$) features a quadrupole doublet centered at a substantially higher isomer shift of 0.49 mm s^{-1} (see below for further discussion of the line shape). Simulations of the NifDK–M($^{57}\text{Fe}_7$), –M($^{57}\text{Fe}_6$), and –M($^{57}\text{Fe}_1$) spectra using the $^{56}\text{Fe}/^{57}\text{Fe}$ ratios obtained from ICP-MS provide the 80 K Mössbauer parameters in Table 1 and Table S7 (see SI for details on the fitting procedure). These data further support the site-selectivity of our labeling protocol and give experimental insights into the electron distribution in the M^{N} state of FeMo-co as discussed below.

Table 1. Mössbauer spectroscopic parameters for the Fe1 site in FeMo-co.

	M^{N}		M^{OX}	
	80 K ^a	4.7 K	80 K	4.7 K
δ (mm s^{-1})	0.49	0.54	0.36	0.36
$ \Delta E_{\text{Q}} $ (mm s^{-1})	0.71	1.33	0.77	0.77
Γ (mm s^{-1})	-	0.42	0.28	0.26

^aValues are reported as an average due to the complex shape of the signal as discussed in the text.

The ENDOR data provide $A(^{57}\text{Fe})$ for the Fe1 site and unequivocally prove that the Fe1 site corresponds to the spectroscopic A^2 site, however the Mössbauer hyperfine parameters for the A^2 site gleaned from analysis of low-temperature (4.2 K) studies on fully labeled samples²⁵ cannot be directly compared to our 80 K Mössbauer studies (*vide supra*). We therefore acquired and analyzed Mössbauer spectra at low temperature (4.7 K). In this temperature regime, the quadrupole doublets for FeMo-co in the M^{N} state are magnetically split with the positions and intensities of the features affected by the presence and orientation of external magnetic fields. We thus collected data in the presence of a weak magnetic

field (77 mT) oriented either parallel or perpendicular to the incident radiation (Fig. 5A). Using the $A(^{57}\text{Fe1})$ hyperfine coupling tensor determined by ^{57}Fe ENDOR spectroscopy and taking into account the background signals from natural-abundance ^{57}Fe in the unlabeled sites of FeMo-co and the P-cluster (gray traces, Fig. 5A; see SI for further discussion), we were able to simulate the signal arising from the Fe1 site and thereby obtain its low-temperature Mössbauer hyperfine parameters: $\delta = 0.54 \text{ mm s}^{-1}$ and $|\Delta E_Q| = 1.33 \text{ mm s}^{-1}$. The spectra can be satisfactorily simulated with either a positive or a negative value for the quadrupole splitting, with a corresponding difference in the Euler angles for the electric field gradient and in the asymmetry parameter for the electric field gradient tensor; the simulations are nearly equivalent (Fig. S6), but the fit is slightly better using $\Delta E_Q = +1.33 \text{ mm s}^{-1}$ and we therefore present the simulations using this value in Fig. 5A. Notably, the values of the isomer shift and the magnitude of the quadrupole

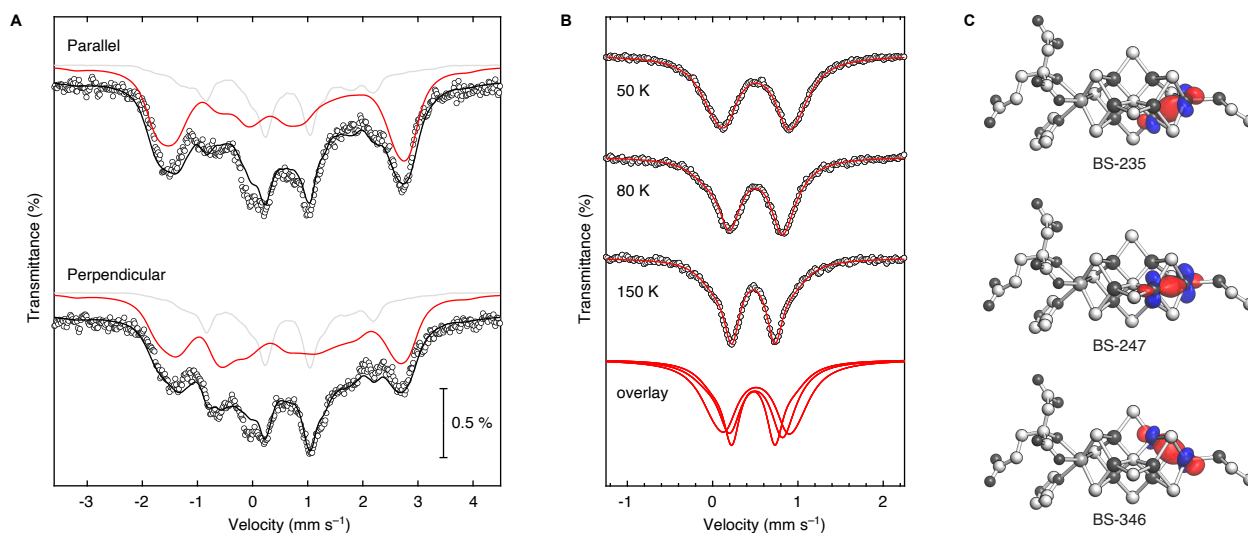


Figure 5. Analysis of the Mössbauer hyperfine parameters for the Fe1 site. A) Mössbauer spectra of the NifDK–M($^{57}\text{Fe}_1$) sample recorded at 4.7 K in the presence of a 77 mT external field oriented parallel (top) or perpendicular (bottom) to the incident radiation. Circles are the experimental data; black traces are the total simulations; red traces are the simulations for the Fe1 site; gray traces are contributions from natural-abundance ^{57}Fe . See SI for simulation details. B) Mössbauer spectra (black circles) of the NifDK–M($^{57}\text{Fe}_1$) sample recorded at various temperatures with all natural-abundance and high spin Fe^{2+} contributions subtracted (see Fig. S3 for the raw data). Each spectrum was fit (red traces) to two quadrupole doublets as described in the SI; the overlays of the fits are presented at the bottom, showing the change in spectral shape and breadth as a function of temperature. C) Isosurface plots (0.05 au) of the localized orbital qualitatively depicting the double exchange interaction between the Fe1 site and the three indicated spin isomers. Hydrogen atoms are omitted for clarity and Cys275 has been truncated.

splitting for the Fe1 site obtained from the site-selectively labeled NifDK–M($^{57}\text{Fe}_1$) sample are higher than those proposed by Yoo *et al.* for any Fe site, including the A^2 site (respectively 0.48 and -0.94 mm s^{-1} at 4.2 K), based on simulations of the fully labeled sample NifDK–M($^{57}\text{Fe}_7$).²⁵ This suggests that the Fe1 site has somewhat more electron density—and, correspondingly, that the six belt Fe sites have somewhat less—than indicated by previous Mössbauer analyses. The implications of this observation are discussed next.

Interpretation of the low-temperature Mössbauer parameters of the Fe1 site in the M^N state

Fe–S clusters have been extensively characterized by Mössbauer spectroscopy,⁴¹ and thiolate-ligated $[\text{Fe}_4\text{S}_4]$ clusters are particularly useful reference compounds for this study because they have an identical primary coordination sphere to that of the Fe1 site of FeMo-co: three μ_3 -sulfides and one Cys-thiolate. For $[\text{Fe}_4\text{S}_4]$ clusters, FeMo-co, and other high-nuclearity Fe–S clusters, the Fe oxidation states are typically assigned as Fe^{2+} , Fe^{3+} , and/or $\text{Fe}^{2.5+}$; the latter corresponds to an Fe in a mixed-valent Fe^{2+} – Fe^{3+} pair in which the excess electron is delocalized via the double-exchange mechanism.^{42,43} Based on comparisons to $[\text{Fe}_4\text{S}_4]$ clusters,⁴¹ the isomer shift and the magnitude of the quadrupole splitting of the Fe1 site of FeMo-co are both too low for an Fe^{2+} site and too high for an Fe^{3+} site. Indeed, they compare favorably to typical values for the $\text{Fe}^{2.5+}$ sites in $[\text{Fe}_4\text{S}_4]^+$ clusters (~ 0.5 and $\sim 1.3 \text{ mm s}^{-1}$, respectively).⁴¹ Furthermore, using an empirical relationship⁴⁴ that relates the formal oxidation state and the Mössbauer isomer shifts of tetrahedral Fe sites in synthetic $\text{FeS}_n(\text{SR})_{4-n}$ compounds, we arrive at an oxidation state of $\text{Fe}^{2.4+}$ for the Fe1 site in M^N . The assignment of an $\text{Fe}^{\sim 2.5+}$ valence is further supported by comparison to the M^{OX} state (*vide infra*), and is broadly consistent with spatially resolved anomalous dispersion (SpReAD)²⁷ and computational^{13,14} analyses that indicate the Fe1 site is relatively reduced.

The identification of an $\text{Fe}^{2.5+}$ oxidation state for the Fe1 site necessitates that one of its neighbors—Fe2, Fe3, or Fe4 (Fig. 1B)—be the other member of the mixed-valent pair. This Fe site must be spin-aligned with Fe1 to undergo electron delocalization via the double exchange mechanism, and it

therefore must be one of the remaining *A* sites, which are each thought to have isomer shifts of ~ 0.4 mm s^{-1} .²⁵ The relatively high isomer shift of the Fe1 site indicates that, on the whole, the covalency of its Fe1–ligand interactions (featuring bonds to three μ_3 -sulfides and one Cys-thiolate) is somewhat lower than that of its double-exchange-coupled partner (featuring bonds to two μ_3 -sulfides, one μ_2 -sulfide, and one μ_6 -carbide). This difference can be attributed at least in part to the greater Fe–S covalency involving μ_2 -sulfides compared with μ_3 -sulfides and thiolates⁴⁵ and may also arise from covalent Fe–C bonding.

In the course of our Mössbauer studies of the NifDK–M(⁵⁷Fe₁) sample, we observed an unexpected temperature dependence to its signal. Although the isomer shift for the Fe1 site behaves as expected—it decreases slightly with increasing temperature, from 0.54 mm s^{-1} at 4.7 K to 0.47 mm s^{-1} at 150 K, a magnitude that is typical for a second-order Doppler shift⁴⁶—the line shape of the signal changes substantially with temperature and is relatively broad even at high temperatures (Fig. 5B). This temperature response is especially apparent in the average quadrupole splitting, which decreases from 1.33 mm s^{-1} at 4.7 K to 0.86, 0.71, and 0.67 mm s^{-1} at 50, 80, and 150 K, respectively (see Table 1 and Table S5 and Fig. 5B). Such behavior cannot be attributed to magnetic relaxation effects; the M^N Mössbauer signal has been shown to be in the fast-relaxation regime at 20 K and above.³² Instead, we ascribe these observations to the thermal population of low-lying excited states with differing quadrupole splitting but essentially invariant isomer shift.

Although the precise molecular basis for this observation is unclear, we note that related high-spin, four-coordinate Fe²⁺ complexes have been observed to exhibit a temperature dependence to their quadrupole splitting.⁴⁷⁻⁴⁹ For these complexes, it has been noted that upon introducing a tetragonal distortion to tetrahedral Fe²⁺, the degeneracy of the two orbitals of *e* parentage (d_{z^2} and $d_{x^2-y^2}$) is lifted; if the splitting of these orbitals is sufficiently small and the temperature is sufficiently high, the β -spin electron can occupy either orbital. Because the two electronic configurations have different electric field gradients, the observed quadrupole splitting changes as the population of these states varies with temperature. This phenomenon has also been used to explain the temperature dependence of the

quadrupole splitting for $\text{Fe}^{2.5+}$ sites in Fe–S clusters in which the delocalized electron occupies the orbitals of e parentage.⁴⁷ It is thus reasonable to propose that the same phenomenon is occurring at the Fe1 site in M^{N} . Moreover, for the Fe1 site in FeMo-co, changing the orientation of the delocalized electron-bearing orbital necessarily changes the identity of its partner spin-aligned Fe site (Fe2, Fe3, or Fe4) with which the electron is delocalized (Fig. 5C), which in turn could cause a rearrangement of the spins throughout the cofactor. Indeed, multiple spin isomers have been predicted to be nearly isoenergetic in several computational studies (*vide infra*);^{10,13,14,50,51} we propose that the temperature dependence of the effective quadrupole splitting and the line shape may arise from thermal population of and interconversion among these (and likely other) electronic states. Notably, this temperature dependence is not readily apparent in Mössbauer spectra of the NifDK– $\text{M}^{(57}\text{Fe}_7)$ sample,²⁵ presumably because such effects are obscured by the severe overlap of the signals from the seven Fe sites. Our findings thereby highlight the power of site-selective labeling in studying high-nuclearity metallocofactors.

The insights from spectroscopic analysis of the site-selectively labeled samples—in particular, that the spin of the Fe1 site is coaligned with the overall electron spin of the cluster, and that the Fe1 site is part of a mixed-valent pair of $\text{Fe}^{2.5+}$ centers—impose new experimental constraints on the electronic structure of FeMo-co in the M^{N} state. All electronic configurations that invoke antiparallel spin alignment between the Fe1 site and the total spin can be rejected; in Noodleman's nomenclature,^{10,52} this includes the BS3, BS6, BS9, and BS10 family of electronic structures. Our results also require that at least one of the neighboring belt Fe sites (Fe2, Fe3, and Fe4) be coaligned with Fe1 in order to engage in electron sharing via the double-exchange mechanism; this further eliminates the BS2 family of electronic structures. Overall, our experimental findings are consistent with the electronic-structure picture favored in recent computational analyses:^{13,14} an $[\text{MoFe}_7\text{S}_9\text{C}]^-$ core charge state and the BS7 family of electronic structures, particularly the three spin isomers BS7-235, BS7-247, and BS7-346, which differ in the identity of the belt Fe that is aligned with the Fe1 site (Fe4, Fe3 and Fe2, respectively; Fig. 5C and *vide supra*).

Mössbauer spectroscopic analysis of the oxidized resting state, M^{OX}

Having the ability to distinguish between the oxidation states of the Fe1 and belt Fe sites, and knowing that the Fe1 site in the M^N state is relatively reduced, we were interested to learn if one-electron oxidation to the M^{OX} state occurs at the Fe1 site, the belt Fe sites, or both. We therefore incubated the NifDK–M(⁵⁷Fe₇), NifDK–M(⁵⁷Fe₆), and NifDK–M(⁵⁷Fe₁) samples with the oxidant phenazine methosulfate (Em₇ = +80 mV vs NHE)⁵³ and ensured that FeMo-co was poised in the M^{OX} state by the absence of the $S = 3/2$ M^N EPR signal (Fig. S9).

The ground spin state of M^{OX} is $S = 0$,^{54,55} and, as such, Mössbauer spectra of FeMo-co in this state do not exhibit magnetic splitting even at low temperature (Fig. 6A and S3). Comparison of the 4.7 K Mössbauer parameters for the Fe1 site in the M^N and M^{OX} states (Table 1) reveals a striking shift in hyperfine parameters: the isomer shift decreases from 0.54 mm s⁻¹ to 0.36 mm s⁻¹ upon FeMo-co

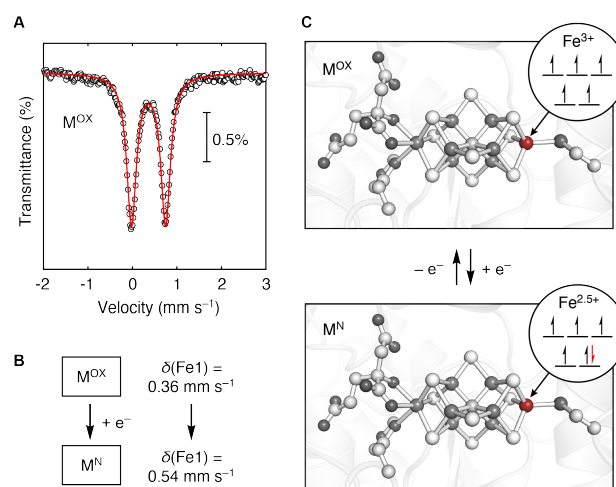


Figure 6. Redox changes at the Fe1 site of FeMo-co. A) Mössbauer spectrum of the oxidized NifDK–M(⁵⁷Fe₁) sample recorded at 4.7 K. Circles are the experimental data; red trace is the simulation for the Fe1 site; contributions from natural-abundance ⁵⁷Fe have been subtracted (see SI). B) Change in isomer shift (4.7 K) for the Fe1 site upon reduction of M^{OX} to M^N. C) Oxidation state of the Fe1 site in M^{OX} (top) and M^N (bottom), where the red electron in the latter represents the electron shared with Fe2, Fe3, or Fe4 via the double exchange mechanism. PDB accession code: 3U7Q⁹

oxidation, and the quadrupole splitting likewise decreases from 1.33 to 0.77 mm s⁻¹. This immediately shows that oxidation of M^N occurs to a large extent at the Fe1 site. Though substantial, the magnitude of the decrease in δ (0.18 mm s⁻¹ at 4.2 K) is smaller than what would be expected for a localized, Fe²⁺ to

Fe^{3+} redox event ($\sim 0.4 \text{ mm s}^{-1}$) and is instead consistent with a conversion of an $\sim \text{Fe}^{2.5+}$ site to an Fe^{3+} site (Table S15).⁴¹ The average isomer shift (80 K) for the belt sites decreases modestly upon oxidation from 0.38 mm s^{-1} in M^{N} to 0.34 mm s^{-1} in M^{OX} . The magnitude of this change ($\sim 0.04 \text{ mm s}^{-1}$ over six sites, or 0.24 mm s^{-1} in total) is likewise consistent with the removal of approximately half an electron from the six belt sites (c.f. the Mössbauer spectra for $[\text{Fe}_4\text{S}_4]^{2+/+}$ clusters, whose isomer shifts differ by $\sim 0.48 \text{ mm s}^{-1}$ per electron when normalized to one site).

Notably, the Mössbauer spectrum of the NifDK- $M(^{57}\text{Fe}_1)$ sample in the M^{OX} state is sharp and symmetrical at both 4.7 K and 80 K (0.26 and 0.28 mm s^{-1} linewidth, respectively), and the quadrupole splitting does not display the temperature dependence observed in the M^{N} state. This further supports our proposal that the temperature-dependence and breadth of the signal in the M^{N} state are electronic in origin and do not reflect, for example, structural heterogeneity in the sample, which would be observed for both the M^{N} and M^{OX} states.

Conclusion

In this paper, we reported a postbiosynthetic, chemical method for site-selective incorporation of ^{57}Fe into FeMo-co and showed how analysis of site-selectively labeled samples yields unprecedented insights into the distribution and coupling of FeMo-co's valence electrons in two redox states, M^{N} and M^{OX} . The ^{57}Fe ENDOR spectroscopic analysis on M^{N} links the crystallographic Fe1 site to the spectroscopic A^2 site, and thereby experimentally connects the electronic properties of an individual site to FeMo-co's geometric structure. We further showed that the Fe1 site is relatively reduced and part of a mixed-valent pair of $\text{Fe}^{2.5+}$ ions. Overall, these findings place new, experimental constraints on the electronic structure of FeMo-co that will inform future computational studies, as well as spectroscopic analyses of the resting state and intermediates.

We also discovered that the mixed-valent pair of $\text{Fe}^{2.5+}$ ions containing the Fe1 site is the site of redox chemistry in the interconversion between M^{N} and M^{OX} and, consequently, that these sites comprise the most reduced moiety in the resting state. Our finding that Fe1 is redox-active, even though it is not thought to be involved in substrate binding,^{3,6,56-58} may indicate a role for this site as a redox reservoir during catalysis. In such a scenario, an electron stored at Fe1 could be deployed in multi-electron steps occurring at other metal sites (*e.g.*, Fe protonation to generate an Fe-hydride, which is a two-electron oxidation).^{56,59-63} Belt Fe sites directly involved in bond-making or -breaking steps would therefore only need to supply a single electron in a two-electron reaction because the additional electron can be derived from the Fe1 site (and its double-exchange-coupled partner). Finally, the ability to observe redox changes in the M^{N} and M^{OX} states using site-selectively labeled samples demonstrates the promise of site-selective isotope editing in characterizing other intermediates and providing new insights into the mechanism of biological nitrogen fixation.

Acknowledgements: We acknowledge the MIT Research Support Committee (to DLMS), the National Institutes of Health (GM111097 to BMH), and the National Science Foundation (MCB-1908587 to BMH) for funding. We thank Niklas Thompson for helpful discussions as well as Dennis Dean and Valerie Cash for providing the *Av* strains used in this work. Support for the ICP-MS instrument was provided by a core center grant P30-ES002109 from the National Institute of Environmental Health Sciences, NIH.

Author contributions: EDB, SS, and DAL performed the experiments; all authors contributed to the design of the study, data analysis, and manuscript writing.

Competing interests: The authors declare no competing interests.

Methods

Cell growth

The *Azotobacter vinelandii* strains DJ1141 (produces His-tagged NifDK), DJ1143 (produces His-tagged apo-NifDK), and wild-type (WT) *A. vinelandii* were cultured in 18 L batches in a 20 L B. Braun Biostat C bioreactor using Burk's minimal medium.

For overproducing holo-NifDK, growths were supplemented with 6 mM ammonium acetate. Derepression was initiated upon ammonium depletion, and cells were harvested after 3 hours.⁶⁴ Cell paste was flash-frozen in LN₂ and stored at -80 °C until purification.

For the culturing of DJ1143, the Burk's minimal medium was supplemented with 10 mM urea. Once the cell density reached an OD₆₀₀ of approximately 4.0, derepression was initiated by resuspending pelleted cells in Burk's minimum medium containing no urea. After 3 hours, the cells were harvested by centrifugation and the cell paste was flash-frozen in LN₂ and stored at -80 °C until needed.

⁵⁷Fe-enriched NifDK protein was generated using identical protocols to what was described above except that the Fe source was generated by dissolving ⁵⁷Fe powder (Trace Science International, 95.5% enrichment) with stoichiometric H₂SO₄.

NifDK purification

All NifDK purification procedures were carried out in a Coy Labs glove box (<5 ppm O₂). All aqueous solutions used were sparged with N₂ overnight. Cells were lysed using the osmotic shock method as followed: DJ1141 cell paste was resuspended with 3 mL of 25 mM HEPES pH 7.5, 50% glycerol, and 2 mM sodium dithionite (DTH) for every gram of cell paste. After stirring at room temperature for 15 minutes, the cells were pelleted at 25,000 × g for 15 minutes. The supernatant was poured off and the pelleted cells were resuspended with 3 mL buffer containing 25 mM HEPES pH 7.5, 2 mM sodium dithionite, 3 mM phenylmethylsulfonyl fluoride (PMSF), 1 mg/mL lysozyme, and 100 µg/mL DNase I for every gram of cell paste. After 15 minutes of stirring, the lysate was pelleted at 100,000 × g for 1 hr

and loaded onto a Co-NTA column equilibrated with buffer containing 500 mM NaCl, 25 mM HEPES pH 7.5, 20% glycerol, and 2 mM DTH. The immobilized protein was washed with 10 column volumes of equilibration buffer and eluted with equilibration buffer containing 200 mM imidazole. NifDK was further purified using anion exchange chromatography: the protein solution was diluted 4-fold with buffer containing 25 mM HEPES pH 7.5, 20% glycerol, and 2 mM DTH and then loaded onto a DEAE-sepharose column charged with NaCl and equilibrated with the dilution buffer. The column was washed with 10 column volumes of 160 mM NaCl, 25 mM HEPES pH 7.5, 2 mM DTH, and 20% glycerol. The immobilized protein was then eluted with buffer containing 500 mM NaCl, 25 mM HEPES pH 7.5, 2 mM DTH, and 20% glycerol. Purified NifDK was concentrated using an AMICON stirred cell equipped with a 30 kDa filter, flash-frozen, and stored in LN₂. The concentration of NifDK was estimated by determining the Mo content using inductively coupled plasma mass spectrometry (ICP-MS).

Note: In our study, the reported concentration of NifDK is based on the $\alpha\beta$ heterodimer concentration (with one FeMo-co per heterodimer in holo-NifDK) rather than the $\alpha_2\beta_2$ heterotetramer concentration (with two FeMo-co per heterotetramer in holo-NifDK).

NifH purification

The purification of NifH was carried out in an MBRAUN glove box (<5 ppm O₂) and was performed similarly to what has been previously reported.⁶⁵ WT *A. vinelandii* cell paste was lysed as described above. Lysate was loaded onto a DE-52 column charged with NaCl and equilibrated in 25 mM HEPES pH 7.5 and 2 mM DTH. The column was washed with a stepwise gradient with buffer containing 125 mM, 200 mM, 300 mM, and 500 mM NaCl. Fractions were analyzed by EPR spectroscopy; those determined to have NifH were pooled and concentrated using a DE-52 cellulose column and AMICON spin filters equipped with a 10 kDa filter. NifH was then purified further using an Superdex 200 column equilibrated with buffer containing 200 mM NaCl, 25 mM HEPES pH 7.5, and 2 mM DTH. Purified NifH

was subsequently concentrated and flash-frozen in LN₂. The concentration of NifH was estimated by UV-vis spectroscopy.⁶⁵

Isolation of FeMo-co

The protocol for FeMo-co isolation was adapted from a previously reported procedure.³³ Protein manipulation was performed in a Coy Labs glove box (<5 ppm O₂) and FeMo-co manipulation was carried out in an MBRAUN or Vacuum Atmospheres glove box (<5 ppm O₂). NifDK (typical protein concentrations ranging from 100 to 400 μM αβ dimer) was diluted 10-fold with aqueous 2 mM DTH. The protein was denatured by the addition of 100 mM citric acid (1.67 mL per 10 mL of diluted protein) added dropwise at 0 °C with stirring. After incubating the mixture for 30 s the protein was precipitated by addition of 200 mM Na₂HPO₄ (1.7 mL per 10 mL of diluted protein). The precipitated protein was transferred to a 15 mL conical tube and moved to the Mbraun box where the protein was pelleted at 120 × g for 5 min using a Labnet Z100A centrifuge. The supernatant was removed and the pellet was washed with *N,N*-dimethylformamide (DMF) (5 mL) and pelleted. This DMF wash step was performed once more. FeMo-co was then extracted by resuspending and vortexing the pellet with 1 to 2 mL of *N*-methylformamide (NMF) containing 2 mM Na₂HPO₄ (from a 200 mM aqueous stock solution). After a 5-minute incubation at room temperature, the extract was centrifuged at 500 × g for 5 minutes, and the brown supernatant was poured off and collected. The process was repeated until the solution was colorless, and the extracts were combined. The concentration of FeMo-co was estimated by UV-vis spectroscopy using an extinction coefficient of PhS-bound FeMo-co in NMF: 14847 M⁻¹ cm⁻¹ at 450 nm (Fig. S7).

Acetylene reduction activity assays

The specific activity of NifDK was assessed using the acetylene reduction activity assay. Assays were performed in 10 mL crimped vials under an atmosphere of 90:10 argon:acetylene in a 30°C water bath. Each assay contained 800 μL of ATP mix (25 mM Tris pH 7.9, 30 mM creatine phosphate disodium

salt, 5 mM ATP disodium salt, 5 mM MgCl₂, 25 units/mL phosphocreatine kinase, and 20 mM sodium dithionite), 100 µg of NifDK, and 435 µg of NifH. Assays were initiated with the addition of NifH and quenched after 6 minutes with 100 µL of 4 M NaOH. Ethylene production was measured by injecting 50 µL of headspace into an Agilent 6890N GC equipped with a flame ionization detector and an HP-PLOT/Q 30 m × 0.319 mm × 20.00 µm column. Ethylene standards were prepared by injecting 1 mL of ethylene into gravimetrically calibrated round bottom flasks containing 1 atm of air.

Post-biosynthetic isotope editing of FeMo-co

Isolated FeMo-co (either ⁵⁷Fe-enriched or natural-abundance) was treated with 30 equiv ethylenediaminetetraacetic acid (EDTA) (added as a 100 mM aqueous stock solution) and stirred at room temperature for 5 minutes. Then 35 equiv FeCl₂ (either natural-abundance or ⁵⁷Fe-enriched) was added (as a 100 mM stock solution in 50% v/v NMF/H₂O), and the solution was stirred for 3 minutes at room temperature. Prolonged incubation of EDTA-treated FeMo-co with FeCl₂ can lead to the appearance of an unidentified $S = 5/2$ EPR signal ($g_{\text{eff}} = 4.3$). However, samples with this signal are competent for insertion of FeMo-co into apo-NifDK, and as such the reaction with excess FeCl₂ appears to be reversible.

Insertion of FeMoco into apo-NifDK protein

The procedure for inserting FeMo-co onto apo-NifDK protein was adapted from previous reports.^{37,38} Excess as-isolated or postbiosynthetically modified FeMo-co (up to 1.5 equiv.) was added dropwise to freshly prepared crude lysate of DJ1143 (lysed using osmotic shock), stirred at room temperature. The final concentration of NMF was approximately 1% v/v. Once FeMo-co addition was complete, the now holo-NifDK protein was purified as described above with an additional step. Following anion exchange chromatography, the NifDK protein was applied to a Superdex 200 column equilibrated in 500 mM NaCl, 25 mM HEPES pH 7.5, 20% glycerol, and 2 mM DTH. Fractions containing NifDK protein were pooled and concentrated. Note: We estimate that 1 g of DJ1143 cell paste grown by the

method described above contains ~10 nmol of apo-NifDK; this value was determined by measuring the yield of apo-NifDK isolated over several purifications from a fixed amount of DJ1143 cell paste.

ENDOR sample preparation

The NifDK–M(⁵⁷Fe₇), NifDK–M(⁵⁷Fe₆), and NifDK–M(⁵⁷Fe₁) samples were prepared as discussed above except for an additional step. Some samples contained small amounts of Co impurities that were likely introduced in the Co-NTA purification step. Although this is not an issue for acquiring Mössbauer data, these impurities can be observed in the EPR spectra. To remove these impurities for ENDOR analysis, the holo-NifDK samples were washed with EDTA several times using the following procedure. Samples (~350 μ L in volume and containing ~100-300 μ M Mo) were washed with EDTA-containing buffer (~10 equiv. per Mo, 500 mM NaCl, 25 mM HEPES pH 7.5, 20% glycerol, and 2 mM DTH) by repeated cycles of concentration and dilution using an AMICON centrifugal spin filter (30 kDa cutoff). Approximately every 5-7 cycles, samples were assessed by EPR to determine if the Co was removed. EDTA was then removed by the same concentration and dilution protocol, but with buffer that did not contain EDTA. This protocol does not affect the intensity or shape of the $S = 3/2$ signal of FeMo-co, though it does lower the specific activity of C₂H₂ reduction to approximately 60 % of the pre-treatment activity (Table S13). The final concentrations for all ⁵⁷Fe ENDOR samples were approximately 100 μ M.

Mössbauer sample preparation

Samples were poised in the M^N state by incubation with DTH. Samples were poised in the M^{OX} state by initial treatment with 500 μ M indigodisulfonate (IDS) and gel filtration into 500 mM NaCl, 25 mM HEPES pH 7.5, and 20% glycerol using a PD-10 column (GE Healthcare). Following gel-filtration, the NifDK sample was fully oxidized by incubating with at least 7 equiv phenazine methosulfate (PMS) (based on Mo concentration) for 3 minutes before freezing in LN₂.

Spectroscopy and spectrometry

Zero-field ^{57}Fe -Mössbauer spectra were recorded with a constant acceleration spectrometer equipped with a JANIS closed cycle He gas refrigerator cryostat. Isomer shifts were quoted relative to α -Fe foil at room temperature. EPR samples were prepared in an anaerobic glove box with an N_2 atmosphere and an O_2 level of <5 ppm. X-band EPR spectra were recorded on a Bruker EMX spectrometer at 9.37 GHz. Q-band ENDOR data were collected using a locally constructed spectrometer.⁶⁶ Inductively coupled plasma mass spectrometer (ICP-MS) data were recorded on an Agilent 7900 ICP-MS instrument. Protein samples were digested with concentrated nitric acid (TraceMetal Grade, Fischer) at 70 °C and were diluted with Milli-Q water to final concentration of 2% nitric acid. Standards for Mo were prepared from a 1000 ppm standard solution (VWR BDH Chemicals). Standards for Fe and ^{56}Fe were prepared from a 1000 ppm standard solution (SPEX Certiprep). Standards for ^{57}Fe were prepared as described previously.²⁸ The concentrations of ^{56}Fe and ^{57}Fe in the standard solutions were based on the natural abundance of each isotope in the unenriched standard (91.7% ^{56}Fe , 2.12% ^{57}Fe) and the isotope enrichment in ^{57}Fe powder (95.5% ^{57}Fe , 3.6% ^{56}Fe).

References

- 1 Raymond, J., Siefert, J. L., Staples, C. R. & Blankenship, R. E. The Natural History of Nitrogen Fixation. *Mol. Biol. Evol.* **21**, 541-554 (2004).
- 2 Canfield, D. E., Glazer, A. N. & Falkowski, P. G. The evolution and future of Earth's nitrogen cycle. *Science* **330**, 192-196 (2010).
- 3 Hoffman, B. M., Lukoyanov, D., Yang, Z.-Y., Dean, D. R. & Seefeldt, L. C. Mechanism of Nitrogen Fixation by Nitrogenase: The Next Stage. *Chem. Rev.* **114**, 4041-4062 (2014).
- 4 Winter, H. C. & Burris, R. H. Nitrogenase. *Annu. Rev. Biochem.* **45**, 409-426 (1976).
- 5 Burgess, B. K. & Lowe, D. J. Mechanism of Molybdenum Nitrogenase. *Chem. Rev.* **96**, 2983-3012 (1996).
- 6 Van Stappen, C. *et al.* The Spectroscopy of Nitrogenases. *Chem. Rev.* **120**, 5005-5081 (2020).
- 7 Einsle, O. & Rees, D. C. Structural Enzymology of Nitrogenase Enzymes. *Chem. Rev.* **120**, 4969-5004 (2020).
- 8 Seefeldt, L. C. *et al.* Reduction of Substrates by Nitrogenases. *Chem. Rev.* **120**, 5082-5106 (2020).
- 9 Spatzal, T. *et al.* Evidence for Interstitial Carbon in Nitrogenase FeMo Cofactor. *Science* **334**, 940 (2011).
- 10 Lovell, T., Li, J., Liu, T., Case, D. A. & Noodleman, L. FeMo Cofactor of Nitrogenase: A Density Functional Study of States M^N , M^{OX} , M^R , and M^I . *J. Am. Chem. Soc.* **123**, 12392-12410 (2001).
- 11 Harris, T. V. & Szilagy, R. K. Comparative Assessment of the Composition and Charge State of Nitrogenase FeMo-Cofactor. *Inorg. Chem.* **50**, 4811-4824 (2011).
- 12 Siegbahn, P. E. M. Model Calculations Suggest that the Central Carbon in the FeMo-Cofactor of Nitrogenase Becomes Protonated in the Process of Nitrogen Fixation. *J. Am. Chem. Soc.* **138**, 10485-10495 (2016).
- 13 Bjornsson, R., Neese, F. & DeBeer, S. Revisiting the Mössbauer Isomer Shifts of the FeMoco Cluster of Nitrogenase and the Cofactor Charge. *Inorg. Chem.* **56**, 1470-1477 (2017).
- 14 Benediktsson, B. & Bjornsson, R. QM/MM Study of the Nitrogenase MoFe Protein Resting State: Broken-Symmetry States, Protonation States, and QM Region Convergence in the FeMoco Active Site. *Inorg. Chem.* **56**, 13417-13429 (2017).
- 15 Raugei, S., Seefeldt, L. C. & Hoffman, B. M. Critical computational analysis illuminates the reductive-elimination mechanism that activates nitrogenase for N_2 reduction. *Proc. Natl. Acad. Sci.* **115**, E10521 (2018).
- 16 Li, Z., Li, J., Dattani, N. S., Umrigar, C. J. & Chan, G. K.-L. The electronic complexity of the ground-state of the FeMo cofactor of nitrogenase as relevant to quantum simulations. *J. Chem. Phys.* **150**, 024302 (2019).
- 17 Cramer, S. P., Hodgson, K. O., Gillum, W. O. & Mortenson, L. E. The molybdenum site of nitrogenase. Preliminary structural evidence from x-ray absorption spectroscopy. *J. Am. Chem. Soc.* **100**, 3398-3407 (1978).
- 18 Cramer, S. P. *et al.* The molybdenum site of nitrogenase. 2. A comparative study of molybdenum-iron proteins and the iron-molybdenum cofactor by x-ray absorption spectroscopy. *J. Am. Chem. Soc.* **100**, 3814-3819 (1978).
- 19 Conradson, S. D. *et al.* Structural insights from the molybdenum K-edge x-ray absorption near edge structure of the iron-molybdenum protein of nitrogenase and its iron-molybdenum cofactor by comparison with synthetic iron-molybdenum-sulfur clusters. *J. Am. Chem. Soc.* **107**, 7935-7940 (1985).
- 20 Venters, R. A. *et al.* ENDOR of the resting state of nitrogenase molybdenum-iron proteins from *Azotobacter vinelandii*, *Klebsiella pneumoniae*, and *Clostridium pasteurianum*. Proton, iron-57, molybdenum-95, and sulfur-33 studies. *J. Am. Chem. Soc.* **108**, 3487-3498 (1986).

- 21 Lukoyanov, D., Yang, Z.-Y., Dean, D. R., Seefeldt, L. C. & Hoffman, B. M. Is Mo involved in hydride binding by the four-electron reduced (E₄) intermediate of the nitrogenase MoFe protein? *J. Am. Chem. Soc.* **132**, 2526-2527 (2010).
- 22 Bjornsson, R. *et al.* Identification of a spin-coupled Mo(III) in the nitrogenase iron–molybdenum cofactor. *Chem. Sci.* **5**, 3096-3103 (2014).
- 23 Van Stappen, C. *et al.* Spectroscopic Description of the E₁ State of Mo Nitrogenase Based on Mo and Fe X-ray Absorption and Mössbauer Studies. *Inorg. Chem.* **58**, 12365-12376 (2019).
- 24 True, A. E., Nelson, M. J., Venters, R. A., Orme-Johnson, W. H. & Hoffman, B. M. Iron-57 hyperfine coupling tensors of the FeMo cluster in *Azotobacter vinelandii* MoFe protein: determination by polycrystalline ENDOR spectroscopy. *J. Am. Chem. Soc.* **110**, 1935-1943 (1988).
- 25 Yoo, S. J., Angove, H. C., Papaefthymiou, V., Burgess, B. K. & Münck, E. Mössbauer Study of the MoFe Protein of Nitrogenase from *Azotobacter vinelandii* Using Selective ⁵⁷Fe Enrichment of the M-Centers. *J. Am. Chem. Soc.* **122**, 4926-4936 (2000).
- 26 Lukoyanov, D. A. *et al.* Electron Redistribution within the Nitrogenase Active Site FeMo-Cofactor During Reductive Elimination of H₂ to Achieve N≡N Triple-Bond Activation. *J. Am. Chem. Soc.* **142**, 21679-21690 (2020).
- 27 Spatzal, T. *et al.* Nitrogenase FeMoco investigated by spatially resolved anomalous dispersion refinement. *Nat. Commun.* **7**, 10902 (2016).
- 28 Srisantitham, S., Badding, E. D. & Suess, D. L. M. Postbiosynthetic modification of a precursor to the nitrogenase iron–molybdenum cofactor. *Proc. Natl. Acad. Sci.* **118**, e2015361118 (2021).
- 29 Ribbe, M. W., Hu, Y., Hodgson, K. O. & Hedman, B. Biosynthesis of Nitrogenase Metalloclusters. *Chem. Rev.* **114**, 4063-4080 (2014).
- 30 Burén, S., Jiménez-Vicente, E., Echavarrri-Erasun, C. & Rubio, L. M. Biosynthesis of Nitrogenase Cofactors. *Chem. Rev.* **120**, 4921-4968 (2020).
- 31 Guo, Y. *et al.* The Nitrogenase FeMo-Cofactor Precursor Formed by NifB Protein: A Diamagnetic Cluster Containing Eight Iron Atoms. *Angew. Chem. Int. Ed.* **55**, 12764-12767 (2016).
- 32 Münck, E. *et al.* Nitrogenase. VIII. Mössbauer and EPR spectroscopy. The MoFe protein component from *Azotobacter vinelandii* OP. *Biochim. Biophys. Acta, Protein Struct.* **400**, 32-53 (1975).
- 33 Shah, V. K. & Brill, W. J. Isolation of an iron-molybdenum cofactor from nitrogenase. *Proc. Natl. Acad. Sci.* **74**, 3249-3253 (1977).
- 34 Rawlings, J. *et al.* Novel metal cluster in the iron-molybdenum cofactor of nitrogenase. Spectroscopic evidence. *J. Biol. Chem.* **253**, 1001-1004 (1978).
- 35 Yang, S. S. *et al.* Iron-molybdenum cofactor from nitrogenase. Modified extraction methods as probes for composition. *J. Biol. Chem.* **257**, 8042-8048 (1982).
- 36 Paustian, T. D., Shah, V. K. & Roberts, G. P. Apodinitrogenase: purification, association with a 20-kilodalton protein, and activation by the iron-molybdenum cofactor in the absence of dinitrogenase reductase. *Biochemistry* **29**, 3515-3522 (1990).
- 37 Christiansen, J., Goodwin, P. J., Lanzilotta, W. N., Seefeldt, L. C. & Dean, D. R. Catalytic and biophysical properties of a nitrogenase Apo-MoFe protein produced by a *nifB*-deletion mutant of *Azotobacter vinelandii*. *Biochemistry* **37**, 12611-12623 (1998).
- 38 McLean, P. A., Papaefthymiou, V., Orme-Johnson, W. H. & Münck, E. Isotopic hybrids of nitrogenase. Mössbauer study of MoFe protein with selective ⁵⁷Fe enrichment of the P-cluster. *J. Biol. Chem.* **262**, 12900-12903 (1987).
- 39 Wink, D. A., McLean, P. A., Hickman, A. B. & Orme-Johnson, W. H. A new method for extraction of iron-molybdenum cofactor (FeMoco) from nitrogenase adsorbed to DEAE-cellulose. 2. Solubilization of FeMoco in a wide range of organic solvents. *Biochemistry* **28**, 9407-9412 (1989).
- 40 McLean, P. A. *et al.* A new method for extraction of iron-molybdenum cofactor (FeMoco) from nitrogenase adsorbed to DEAE-cellulose. 1. Effects of anions, cations, and preextraction treatments. *Biochemistry* **28**, 9402-9406 (1989).

- 41 Pandelia, M.-E., Lanz, N. D., Booker, S. J. & Krebs, C. Mössbauer spectroscopy of Fe/S proteins. *Biochim. Biophys. Acta, Mol. Cell Res.* **1853**, 1395-1405 (2015).
- 42 Papaefthymiou, V., Girerd, J. J., Moura, I., Moura, J. J. G. & Muenck, E. Moessbauer study of *D. gigas* ferredoxin II and spin-coupling model for Fe₃S₄ cluster with valence delocalization. *J. Am. Chem. Soc.* **109**, 4703-4710 (1987).
- 43 Noodleman, L. Exchange coupling and resonance delocalization in reduced iron-sulfur [Fe₄S₄]⁺ and iron-selenium [Fe₄Se₄]⁺ clusters. 1. Basic theory of spin-state energies and EPR and hyperfine properties. *Inorg. Chem.* **30**, 246-256 (1991).
- 44 Venkateswara Rao, P. & Holm, R. H. Synthetic Analogues of the Active Sites of Iron–Sulfur Proteins. *Chem. Rev.* **104**, 527-560 (2004).
- 45 Solomon, E. I., Gorelsky, S. I. & Dey, A. Metal–thiolate bonds in bioinorganic chemistry. *J. Comput. Chem.* **27**, 1415-1428 (2006).
- 46 Gütllich, P., Bill, E. & Trautwein, A. X. *Mössbauer spectroscopy and transition metal chemistry: fundamentals and applications*. (Springer-Verlag, 2011).
- 47 Silver, J. *et al.* Effects of Temperature and Pressure on the Mössbauer Spectra of Models for the [4Fe-4S]²⁺ Clusters of Iron–Sulfur Proteins and the Structure of [PPh₄]₂[Fe₄S₄(SCH₂CO₂C₂H₅)₄]. *Inorg. Chem.* **38**, 4256-4261 (1999).
- 48 Edwards, P. R., Johnson, C. E. & Williams, R. J. P. Mössbauer Spectra of Some Tetrahedral Iron (II) Compounds. *J. Chem. Phys.* **47**, 2074-2082 (1967).
- 49 Dunham, W. R. *et al.* The two-iron ferredoxins in spinach, parsley, pig adrenal cortex, *Azotobacter vinelandii*, and *Clostridium pasteurianum*: Studies by magnetic field Mössbauer spectroscopy. *Biochim. Biophys. Acta, Bioenerg.* **253**, 134-152 (1971).
- 50 Lovell, T. *et al.* Metal Substitution in the Active Site of Nitrogenase MFe₇S₉ (M = Mo⁴⁺, V³⁺, Fe³⁺). *Inorg. Chem.* **41**, 5744-5753 (2002).
- 51 Lovell, T., Li, J., Case, D. A. & Noodleman, L. FeMo cofactor of nitrogenase: energetics and local interactions in the protein environment. *J. Biol. Inorg. Chem.* **7**, 735-749 (2002).
- 52 Lukoyanov, D. *et al.* Testing if the Interstitial Atom, X, of the Nitrogenase Molybdenum–Iron Cofactor Is N or C: ENDOR, ESEEM, and DFT Studies of the *S* = 3/2 Resting State in Multiple Environments. *Inorg. Chem.* **46**, 11437-11449 (2007).
- 53 Wilson, G. S. in *Methods in Enzymology* Vol. 54 396-410 (Academic Press, 1978).
- 54 Zimmermann, R. *et al.* Nitrogenase X: Mössbauer and EPR studies on reversibly oxidized MoFe protein from *Azotobacter vinelandii* OP. Nature of the iron centers. *Biochim. Biophys. Acta, Protein Struct.* **537**, 185-207 (1978).
- 55 Johnson, M. K., Thomson, A. J., Robinson, A. E. & Smith, B. E. Characterization of the paramagnetic centres of the molybdenum-iron protein of nitrogenase from *Klebsiella pneumoniae* using low temperature magnetic circular dichroism spectroscopy. *Biochim. Biophys. Acta, Protein Struct.* **671**, 61-70 (1981).
- 56 Igarashi, R. Y. *et al.* Trapping H[•] Bound to the Nitrogenase FeMo-Cofactor Active Site during H₂ Evolution: Characterization by ENDOR Spectroscopy. *J. Am. Chem. Soc.* **127**, 6231-6241 (2005).
- 57 Seefeldt, L. C., Hoffman, B. M. & Dean, D. R. Mechanism of Mo-dependent nitrogenase. *Annu. Rev. Biochem.* **78**, 701-722 (2009).
- 58 Spatzal, T., Perez, K. A., Einsle, O., Howard, J. B. & Rees, D. C. Ligand binding to the FeMo-cofactor: structures of CO-bound and reactivated nitrogenase. *Science* **345**, 1620-1623 (2014).
- 59 Lukoyanov, D., Barney, B. M., Dean, D. R., Seefeldt, L. C. & Hoffman, B. M. Connecting Nitrogenase Intermediates with the Kinetic Scheme for N₂ Reduction by a Relaxation Protocol and Identification of the N₂ Binding State. *Proc. Natl. Acad. Sci.* **104**, 1451 (2007).
- 60 Doan, P. E. *et al.* ⁵⁷Fe ENDOR spectroscopy and 'electron inventory' analysis of the nitrogenase E₄ intermediate suggest the metal-ion core of FeMo-cofactor cycles through only one redox couple. *J. Am. Chem. Soc.* **133**, 17329-17340 (2011).

- 61 Lukoyanov, D. *et al.* Identification of a Key Catalytic Intermediate Demonstrates That Nitrogenase Is Activated by the Reversible Exchange of N₂ for H₂. *J. Am. Chem. Soc.* **137**, 3610-3615 (2015).
- 62 Lukoyanov, D. *et al.* Reductive Elimination of H₂ Activates Nitrogenase to Reduce the N≡N Triple Bond: Characterization of the E₄(4H) Janus Intermediate in Wild-Type Enzyme. *J. Am. Chem. Soc.* **138**, 10674-10683 (2016).
- 63 Harris, D. F. *et al.* Mechanism of N₂ Reduction Catalyzed by Fe-Nitrogenase Involves Reductive Elimination of H₂. *Biochemistry* **57**, 701-710 (2018).
- 64 Lee, C.-C., Ribbe, M. W. & Hu, Y. in *Metalloproteins: Methods and Protocols* (ed Yilin Hu) 111-124 (Springer New York, 2019).
- 65 Burgess, B. K., Jacobs, D. B. & Stiefel, E. I. Large-scale purification of high activity *Azotobacter vinelandII* nitrogenase. *Biochim. Biophys. Acta, Enzymol.* **614**, 196-209 (1980).
- 66 Davoust, C. E., Doan, P. E. & Hoffman, B. M. Q-Band Pulsed Electron Spin-Echo Spectrometer and Its Application to ENDOR and ESEEM. *J. Magn. Reson., Ser. A* **119**, 38-44 (1996).